



Adsorptive Mechanism of Chromium Adsorption on Siltstone–Nanomagnetite–Biochar Composite

Salah Ud Din¹ · Muhammad Sarfraz Khan¹ · Sajjad Hussain^{2,3} · Muhammad Imran⁴ · Sirajul Haq¹ · Muhammad Hafeez¹ · Zain-ul-Abdin¹ · Fazal Ur Rehman¹ · Xuenian Chen³

Received: 23 August 2020 / Accepted: 23 November 2020 / Published online: 1 January 2021
© Springer Science+Business Media, LLC, part of Springer Nature 2021

Abstract

In this work, the potential of a novel and highly efficient composite of *Eleocharis dulcis* biochar with magnetite nanoparticles and siltstone was explored for removing chromium from water. Characterization of the prepared biochar composite was carried out using thermal gravimetric analysis (TGA), X-ray photon spectroscopy (XPS), X-ray diffraction (XRD), Fourier transform infrared spectroscopy (FTIR) and transmission electron microscopy, point of zero charge and BET. XRD confirmed magnetite and quartz to be the main phases in biochar composite. TGA results showed higher thermal stability of the composite after the addition of siltstone. Batch adsorption mode was employed for studying the adsorption capacity of sample for the decontamination of chromium as a function of concentrations, time, temperatures and pHs. Kinetic modelling confirmed pseudo second order to fit best to the kinetic data for chromium adsorption on the composite biochar. An increase of adsorption was observed with the rise in temperature from 303 to 318 K showing the endothermic nature of the process whereas pH study showed higher removal efficiency of chromium in the acidic pH range. Langmuir model was applicable to the data with higher value of correlation. The thermodynamic parameter ΔH° (40.46 kJ mol⁻¹) and negative but higher values of (ΔG°) shows the endothermic and spontaneous nature of the adsorption process respectively. Higher value of activation energy (15.08 kJ mol⁻¹) confirmed the chemical nature of the process. Post adsorption FTIR and XPS confirmed the adsorption of chromium on the surface of the composite. The adsorption capacity obtained in the present study was found to be higher as compared to many other reported adsorbents used for chromium removal.

Keywords Siltstone · Adsorption · Biochar · Chromium

Supplementary Information The online version of this article (<https://doi.org/10.1007/s10904-020-01829-7>) contains supplementary material, which is available to authorized users.

✉ Salah Ud Din
salah.mahsud@ajku.edu.pk

¹ Department of Chemistry, University of Azad Jammu and Kashmir, Muzaffarabad, Azad Kashmir 13100, Pakistan

² School of Chemistry, Faculty of Science, Minhaj University, Lahore, Pakistan

³ School of Chemistry and Chemical Engineering, Henan Key Laboratory of Boron Chemistry and Advanced Energy Materials, Henan Normal University, Xixiang 453007, China

⁴ Department of Environmental Sciences, COMSATS University Islamabad, Vehari Campus, Vehari 61100, Pakistan

1 Introduction

Rapid industrialization has adversely affected human health due to the direct discharge of chromium from industries into the water resources which are allocated for human drinking thereby making it a global challenge for scientists around the world [1]. The main sources responsible for discharge of chromium into water includes tanning, textile manufacturing, steel manufacturing, paints and electroplating. Hexavalent chromium is much more hazardous than Cr(III) as it is mutagenic, carcinogenic and also responsible for lung cancer, diarrhea, vomiting, enzyme inhibition and leukemia [2, 3].

Of all the other techniques commonly used for heavy metals removal such as flocculation, reverse osmosis and coagulation etc., adsorption is an effective technique for removing Cr(VI) due to its high efficiency, simplicity and cost [4–6]. Various adsorbents are used for the

decontamination of heavy metals such as, alumina, magnetic polypyrrole composite nanofibers, iron oxide, mxene/alginate composites, zirconia, waste carton-derived nanocomposites, activated carbon, carbon nanotubes, C-4-hydroxy-3-methoxyphen-ylcalix resorcinarene, polypyrrole/chitosan nanocomposite aerogel monolith [7–18], but most of these adsorbents are high in cost, involves complex methods of synthesis and cause secondary pollution [5].

The heterogeneous and porous structure of biochar have attracted researchers for its use as an adsorbent for the removal of heavy metals from water. However, powdered biochar is difficult to be separated from the aqueous medium after adsorption. This arises the need to modify biochar for its easy separation from water after adsorption [19].

Similarly, magnetite iron oxide nanoparticles have also been extensively used for water decontamination due to their small size particles, easy magnetic separation, larger surface areas and reusability [20]. However, the use of iron oxide nanoparticles for water decontamination is limited on the ground of its eco-toxicity and safety which is still a matter of continuous investigation. Therefore the development of composites of iron oxide with other materials combining the less reactive role of iron oxide nanoparticles to avoid its eco-toxicity and hazardousness together with its easy magnetic separation from the water is better suited for application in water industry. Thus, composite of biochar with magnetite nanoparticles, to make it magnetic for its easy separation from aqueous medium using an external magnetic field, can be a good choice in this context. Still, the leaching of iron oxide nanoparticles back to the aqueous medium as a source of secondary pollution during adsorption process is an issue of concern [21]. To overcome this limitation of magnetite biochar, another layer of a material that can retard the release of Fe ions is needed.

The present study therefore utilizes the potential of siltstone as an external protector for magnetite biochar to minimize its adverse effect on the environment. Siltstone mainly consists of quartz along with other minerals and it contains multifunctional groups which can efficiently uptake the dissolved metal ions. Moreover, siltstone contains many pores and cavities on its surface [22] which maintains the adsorption capacity of biochar for heavy metals removal. The biochar for this composite is synthesized from a locally available edible plant *Eleocharis Dulcis* which is used for the first time for chromium removal. This plant is commonly known as water chestnut and belongs to Cyperaceae family. To the best of our knowledge, the detailed applicability of magnetite biochar composites with siltstone for removal of chromium has not yet been explored and this study is first of its kind.

2 Experimental

2.1 Glassware and Solutions

The glassware used were rinsed with dilute nitric acid and washed with distilled water afterwards. Analytical grade chemicals were used for the preparation of samples/solutions.

2.2 Preparation of *Eleocharis dulcis* Biochar (EDB)

Dust particles and impurities were removed from the bark of *Eleocharis dulcis* (ED) by washing three times with tap water. Then washing of the bark was accomplished by distilled water and then the bark was dried in the air. Then, the bark was boiled in water and dried at 105 °C for 24 h in an oven. The sample was pyrolyzed in a furnace in the absence of oxygen. The temperature of the pyrolysis was increased with the heating speed of 8 °C min⁻¹ until it reached upto 400 °C and held for 1 h. After that it was cooled. The synthesized EDB was finally ground to very fine particles and it was stored in plastic bags.

2.3 Preparation of Magnetic Nanoparticle (MNPs)

Magnetite nanoparticles were synthesized by a method reported elsewhere [10, 23]. To synthesize magnetite nanoparticles, 8 mL of 14% solution of FeSO₄·7H₂O (Sigma-Aldrich) and 4 mL of 13.5% solution of FeCl₃·6H₂O (Sigma-Aldrich) were mixed thoroughly for 10 min and then mixture was titrated with 60 mL of 6% ammonia solution (Merck) with continuous shaking. The color of the solution turned yellow by the addition of iron precursor and then gradually changed to dark black by the addition of ammonia solution showing the formation of magnetic iron oxide nanoparticle. The synthesized nanoparticles thus formed were kept in an oven at 100 °C for 36 h.

2.4 Preparation of Biochar Composite with Magnetite and Siltstone (EDB/MNPs/SS)

Composite (MBS) of EDB with MNPs and siltstone (a sedimentary rock) was synthesized by mixing with 0.7 g of finally divided powdered siltstone and 0.7 g of EDB in 6 mL of 4% (w/v) FeSO₄·7H₂O and 8 mL of 13.5% (w/v) FeCl₃·6H₂O solution in beaker. The synthesized siltstone nanomagnetite biochar composite was filtered and then at 100 °C, it was oven dried. Then the composite was calcined for 60 min in a furnace at 300 °C and for its further

application to remove Cr from contaminated water, the composite was then stored in plastic bags.

2.5 Material Characterization

Infrared spectra of the biochar composite were recorded in between 400 and 4000 cm^{-1} by using 640 IR spectrophotometer for the structural and functional groups determination. For FTIR examination, potassium bromide (KBr) pellet method was applied. Analysis of the crystalline phase of the sample was performed by X-ray diffraction (XRD), by using Bruker D8 Advance diffractometer which was operational with $\text{CuK}\alpha$ radiation ($\lambda = 1.5406 \text{ nm}$) and in the range of 2θ from 10 to 60. Identification of phase was carried out by comparing it with standard cards using XPERT High Score software. Morphology of the sample was determined by using Scanning Electron Microscopy (SEM) JSM 6700S which works in a high vacuum at 5.0 kV with an emission current of 9000 nA and filament current of 0.00184 mA. Transmission electron microscope (JEOL JEM- 2100) was used to determine the size of the composite material. A histogram was plotted by Image J software and origin pro to find out the particle size using TEM images. X-ray photon spectroscopy was performed by using PHI 5100 series ESCA spectrometer for the analysis of oxidation state and composition of the composite. Thermal gravimetric analysis (TGA) and differential calorimetric (DSC) were recorded by using Shimadzu TGA-50 instrument to find out the thermal stability of biochar composite. Heating was done from 30 to 1000 $^{\circ}\text{C}$ and volumetric flow rate of nitrogen was 40 mL min^{-1} . PZC of biochar composite was calculated by a known method reported in literature [24]. Forty milliliter of 0.1 M NaCl solutions were taken in different flasks and their initial pH was adjusted between pH 3.00 and 11.00 by adding suitable amounts of 0.1 M HCl/NaOH solutions. 0.1 g of the EDB composite was added to each flask and then continuous stirring was carried out for about 24 h by using shaker bath (GFL-1086) at room temperature. Final pH was recorded after 24 h of shaking and difference between final and initial pH was recorded. From the plot of ΔpH versus initial pH, PZC values were calculated.

2.6 Adsorption Studies of Chromium on Biochar Composite

Adsorption experiments of Cr(VI) on biochar composite was performed using batch mode. The effect of concentrations, pH and temperature was studied. MBS (0.1 g) was added to flasks containing 40 mL of Cr(VI) solutions in the concentration range of 10 to 100 mg L^{-1} . In order to study the influence of temperature on the adsorption system, same concentration range and adsorbent dosage was used at temperature of 303 to 318 K. 70 mg L^{-1} of the

Cr(VI) solutions were taken in different flasks and their initial pH was varied between 2 to 8 to study the effect of pH whereas the temperature of the system in the pH study was maintained at 303 K. 0.1 M NaOH/ HNO_3 was used to adjust the initial pH of flasks which were then kept in a shaker bath at 120 rpm for 24 h to achieve the equilibrium time. The final pH of the samples was recorded after they were taken out of the shaker bath, magnetically decanted and then by using Whatman filter paper, these solutions were filtered. After that, this filtrate was placed into bottles and concentration of residual chromium was analyzed by using atomic adsorption spectrophotometer.

2.7 Adsorption Kinetics

Kinetic study of adsorption of Cr(VI) ions on the biochar composite was studied using batch technique. Forty mL of 70 mg L^{-1} of the corresponding metal solution was taken in different flasks and 0.1 g of adsorbent was taken in each flask. Then pH of these flasks was maintained at 0.7 using 0.1 M NaOH/ HNO_3 . These samples were afterwards shaken in a shaker bath at 120 rpm at temperatures of 303, 308, 313 and 318 K. These samples were then taken out from the shaker bath after various intervals, magnetically decanted and then filtered by using Whatman filter paper No. 43 after which their final pH was noted. These filtrate were then poured in bottles for onward analysis of residual chromium concentration using atomic adsorption spectrophotometer.

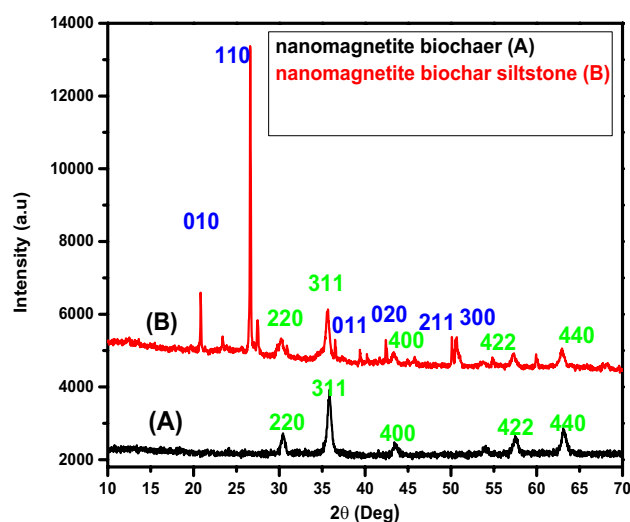


Fig. 1 XRD spectra of nanomagnetite biochar (a) and composite of nanomagnetite biochar with siltstone (b)

3 Results and Discussion

3.1 X-ray Diffraction Analysis (XRD) and BET

XRD pattern of biochar composite with magnetite and siltstone is shown in Fig. 1. The crystalline nature of biochar composite was confirmed by appearance of peaks in the XRD spectrum. The analysis of the XRD data using XPERT high score software showed quartz to be the major component in the siltstone and it appeared along with magnetite in the biochar composite. The diffraction peaks at $2\theta = 30.0^\circ$, 35.5° , 44.0° , 56.3° and 62.5° were indexed as (220), (311), (400), (422) and (440) respectively and these peaks matched with JCPDS card No 19-0619 for magnetite. Similarly, the peaks at $2\theta = 20.33^\circ$, 26.66° , 36.5° , 42.40° , 50.108° and 50.642° with miller indices (010), (110), (011), (020), (211) and (300) respectively were confirmed for quartz according to JCPDS card No 41-1445. The crystallite size calculated using the well-known Scherer formula was 18.5 nm which lies well within the nano range.

The BET surface area for the composite of magnetite biochar composite with siltstone was found to be $62.31 \text{ m}^2 \text{ g}^{-1}$.

3.2 Fourier Transform Infrared (FTIR) Analysis

The composite of magnetite biochar with siltstone was subjected to FTIR analysis in the range of $4000\text{--}400 \text{ cm}^{-1}$ (Fig. 2). Various bands in the spectra indicates the existence of different functional groups in the composite sample. The spectra showed a wide band at $3400\text{--}3500 \text{ cm}^{-1}$ indicating the adsorbed water molecule whereas peaks around 1725 cm^{-1} and 1642 cm^{-1} (Fig. 2a) are attributed

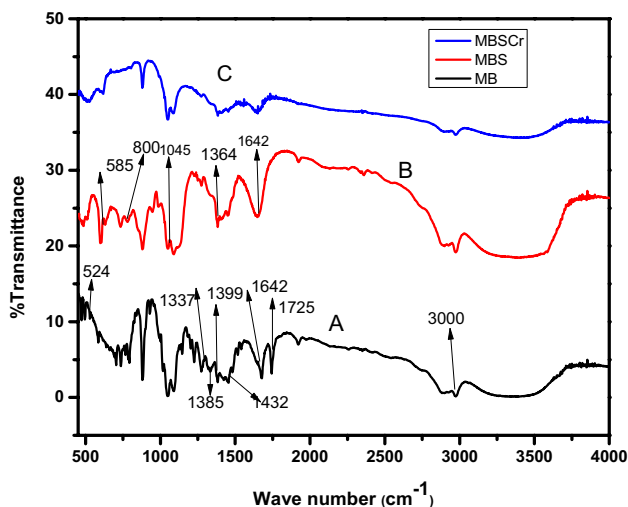


Fig. 2 FTIR spectra of nanomagnetite biochar (a), nanomagnetite biochar with siltstone (b) and chromium loaded MBS (c)

to carbonyl and carboxyl $\text{C}=\text{O}$ groups respectively [25]. The bands appearing at 1337 and 1399 cm^{-1} are assigned to aliphatic (C-H) folding. A narrow sharp peak at 2928 and 3000 cm^{-1} shows the presence of aliphatic $-\text{CH}$ stretch. The stretching vibrations of COO^- appeared at 1385 cm^{-1} . The peak at 1432 cm^{-1} shows aromatic $\text{C}=\text{C}$ stretch. A small peak at 1337 cm^{-1} was slightly shifted to a more clear peak at 1364 cm^{-1} (Fig. 2b) which shows the stretch of carboxylate ions [26–28]. The peak at 524 cm^{-1} shows the stretch of FeO which confirms the impregnation of magnetite on biochar surface. After coating with siltstone, the peak of FeO is also shifted from 524 to 585 cm^{-1} and became broader indicating new interaction between iron and siltstone [29]. The stretching vibrations of Si-O appeared at 1045 cm^{-1} while the peak for silicon dioxide O-Si-O appeared at 800 cm^{-1} [30].

3.3 Scanning Electron Microscopy (SEM)

Both magnetite biochar (MB) and composite of magnetite biochar with siltstone (MBS) were subjected to the SEM analysis and corresponding micrograph are shown in Fig. 3. The surfaces of both the samples appear to be rough and porous. The particles are irregular in shape and are aggregated due to surface energies and magnetism. However, as can be seen from the Figure, the particles of MBS are

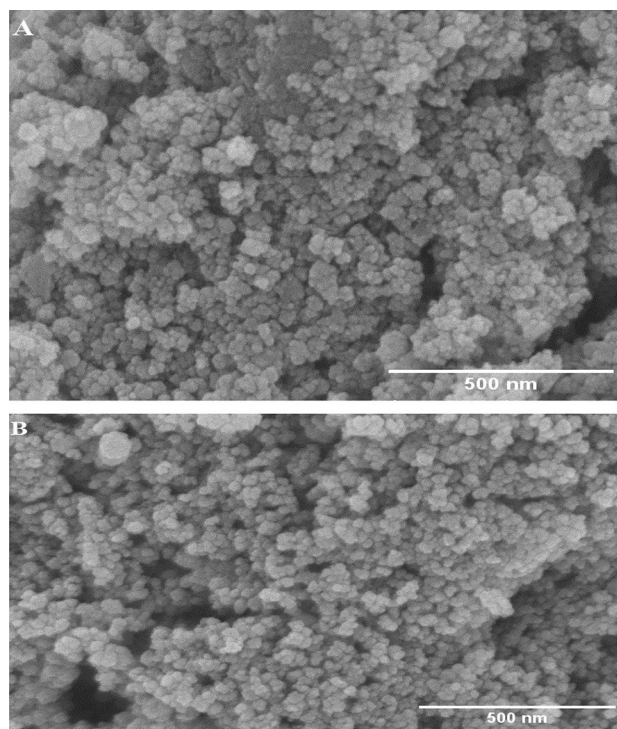


Fig. 3 SEM micrograph of nanomagnetite biochar (a) nanomagnetite biochar with siltstone (b)

less aggregated as compared to MB particles. This reduced agglomeration of MBS particles as compared to MB particles can be attributed to the addition of siltstone which resulted in better dispersion in MBS. Similar decrease in aggregation of particles has been reported elsewhere [31].

3.4 Transmission Electron Microscopy (TEM)

TEM analysis of sample was carried out to calculate the particle size of the samples. TEM micrograph are shown in Fig. 4 which shows that the MBS particles are less aggregated as compared to MB particles. The average size of the particles of the magnetite biochar composite with siltstone was measured from TEM micrographs using image J software and was approximately 22 nm as shown in Fig. 5. This value of particle size is closer to the crystallite size of sample calculated using XRD data (18.5 nm).

3.5 X-ray Photon Spectroscopy (XPS)

The XPS full survey scan of MBS in the range of 0–1200 eV is shown in Fig. 6a while the Fe 2p, C 1s, O 1s and Si 2p spectra are also shown in Fig. 6b to e. Those peaks that appeared on 710.6, 283.8, 531.2 and 102.5 eV shows binding energies of iron, carbon, oxygen and silicon respectively (Fig. 6a). The peaks at 710.6 eV is broad and is further deconvoluted into three peaks (Fig. 6b). Fe 2p_{3/2} and Fe 2p_{1/2} peaks appeared at 710.9 and 724.5 eV respectively

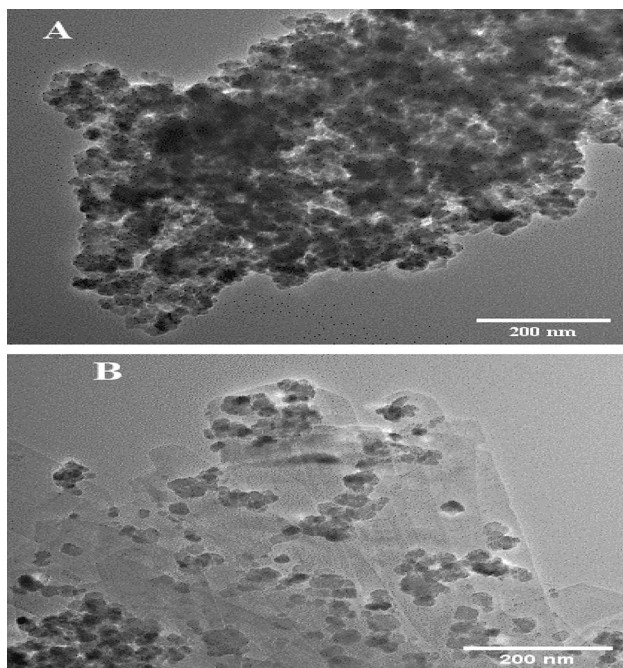


Fig. 4 TEM images of nanomagnetite biochar (a) and nanomagnetite biochar with siltstone (b)

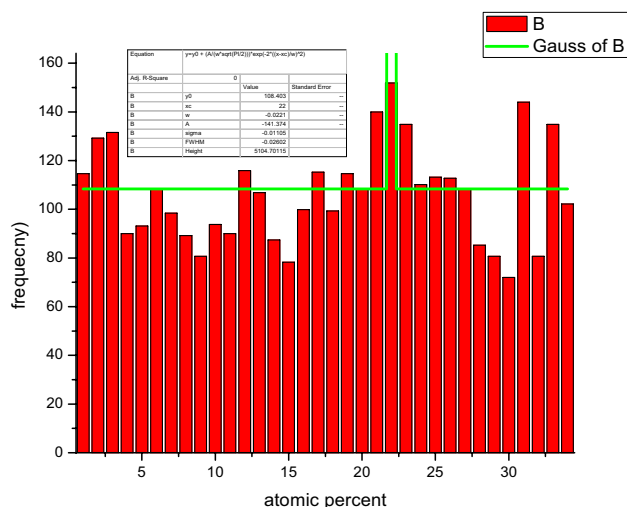


Fig. 5 Histogram by image J software of nanomagnetite biochar with siltstone

and are the characteristics peaks of magnetite [32]. The peaks at 711.45 eV shows Fe(III) whereas Fe(II) appears at 719.86 eV. The peak of C 1s was observed at 283.8 eV (Fig. 6c). This peak was further deconvoluted into four peaks. These peaks at 284.6 eV, 284.8 eV, 286.8 eV and 288.8 eV are for C–H/C–C, C=C, hydroxyl, epoxy (C–O) and carboxylate (O=C–O) respectively [6, 32–34]. Peak at 530 eV is of O 1s. The peaks appearing at 531.1 eV and 532.3 eV (Fig. 6d) shows the C–O and OH⁻¹ groups respectively which indicates that oxygen has captured electron in the empty spaces of biochar surface [35–38]. The broad peak at 102.5 eV (Fig. 6e) represents Si 2p scan and is further deconvoluted into two peaks at 102.7 eV and 103.6 eV attributed to SiO and SiO₂ respectively. A narrow peak appearing at 99.6 eV is of silicon. The integrated areas of these curves clearly indicates that Si is successfully incorporated on the MB surface as 82% SiO₂, 13% SiO and 5% Si [39].

3.6 Thermal Gravimetric Analysis/Differential Scanning Calorimetry (TGA/DSC)

The thermal stability of MBS and MB was investigated using thermal gravimetric analysis and is shown in Fig. 7a, b. In the temperature ranges from 25 to 120 °C, initial weight loss of 3% was observed which was due to the vaporization of water absorbed as free bounded water. A second weight loss of 8% in the range of 200 to 480 °C was due to the vaporization of pore bounded water whereas a third weight loss of 20% up to 800 °C may be attributed to the loss of covalently bonded water [40]. Further weight loss after this temperature reaching up to a total of 25% of initial weight is attributed to the decomposition of lignin

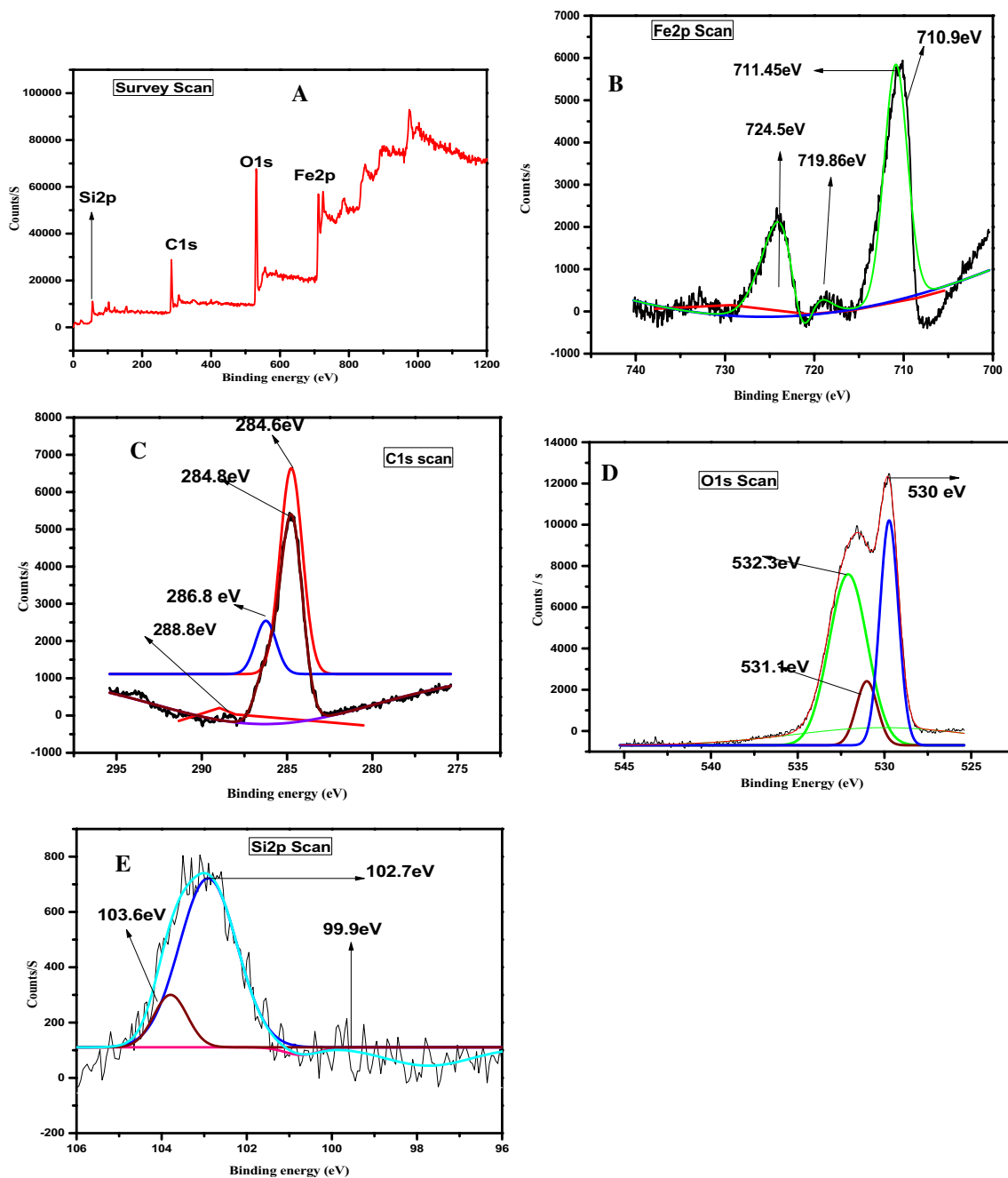


Fig. 6 XPS survey scan of magnetite biochar composite with siltstone (a), Fe2p (b), C1s (c), O1s (d) and Si2p (e)

[41]. The total weight loss is supported by a broad DSC curve and the humps in the DSC curve exactly matches the pattern in the weight loss curve. A comparative look at the thermal stabilities of MB and MBS (Fig. 7a, b) shows higher thermal stability and lower weight loss of 25% for MBS as compared to MB with weight loss of 40% up to a temperature of 1000 °C. This shows higher thermal stability of magnetite biochar with the addition of siltstone.

3.7 Point of Zero Charge (PZC)

The pH at which adsorbent surface has zero charge is called point of zero charge (PZC). A plot of initial pH verses change of pH was plotted and the PZC was thereby calculated to be 6.77 as shown in Fig. 8 which is favorable for adsorption of anionic pollutants like chromium.

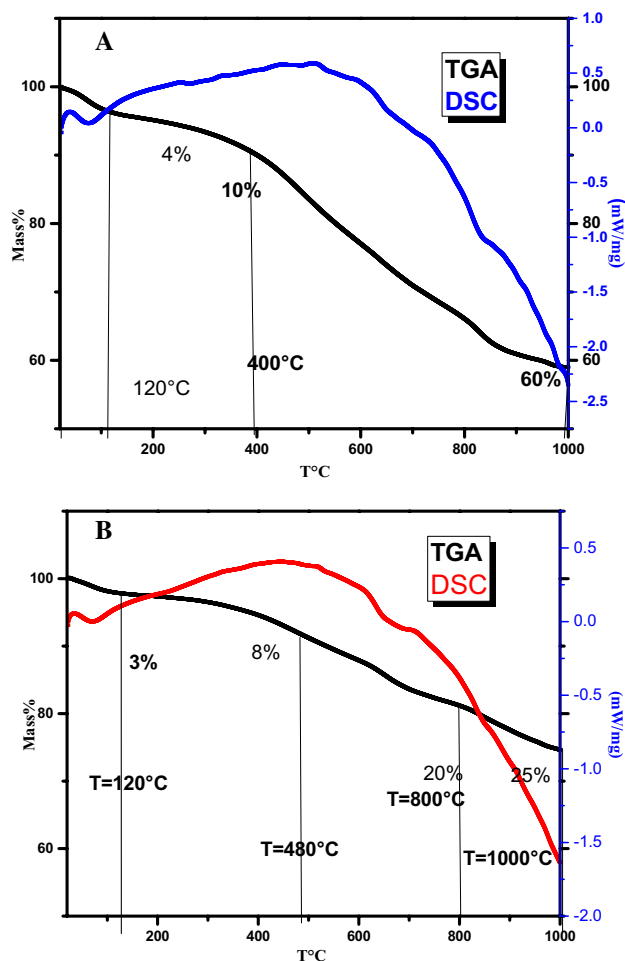


Fig. 7 TGA/DSC plots of nanomagnetite biochar (a) and nanomagnetite biochar with siltstone (b)

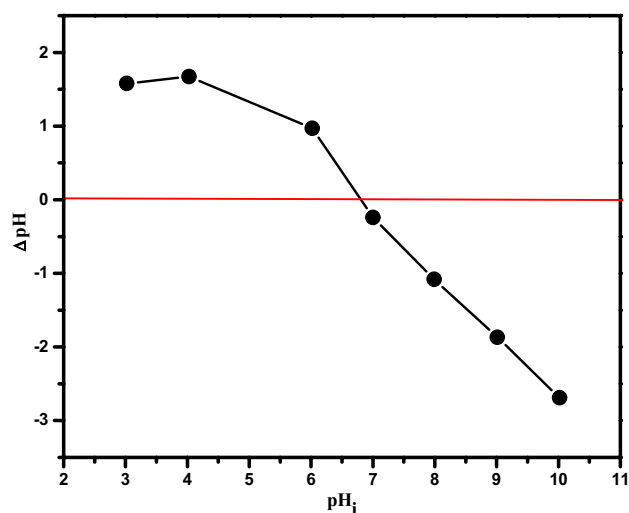


Fig. 8 Point of zero charge of nanomagnetite biochar with siltstone at 303 K

3.8 Adsorption Kinetics of Chromium

3.8.1 Effect of Contact Time on Chromium Ions Adsorption

The adsorption of Cr(VI) ions as a function of time was studied with initial 70 mg L^{-1} concentration and at temperatures of 303 K, 308 K, 313 K and 318 K. The pH was maintained at 7 to represent the ground water pH. A graph of adsorbed Cr(VI) ions with contact time is shown in Fig. 9. As is clear from the graph, there was faster adsorption of chromium in the first 60 min after which the adsorption slows down significantly in later hours leading to equilibrium condition in 240 min. This faster adsorption in the initial 60 min is due to more available surface sites which later on decrease with time and the chromate ions have to compete for the remaining lower number of sites in the later hours [37].

3.9 Kinetic Modelling

The linear form of pseudo first order is expressed as follows,

$$\log(qe - qt) = \log(qe) - k/2.303t \quad (1)$$

In this equation qt is the amount of metal ions adsorbed (mol g^{-1}) at time t and qe is the amount of metal ions adsorbed (mol g^{-1}) at equilibrium while k is the pseudo first order rate constant. A graph of $\log(qe - qt)$ against time (t) gives a straight line (Fig. S1). The graph did not follow linearity which shows that chromium adsorption on magnetite biochar composite does not follow pseudo first order equation.

The kinetics data was then subjected to pseudo second order rate equation. The linearized form of pseudo second order rate equation is expressed as below:

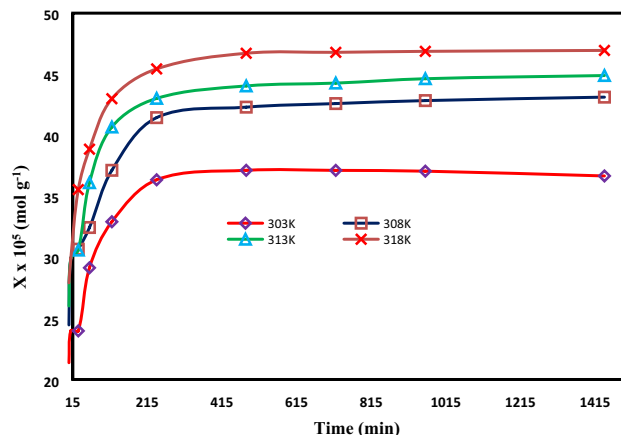


Fig. 9 Effect of contact time on the adsorption of chromium at 303 K, 308 K, 313 K and 318 K on nanomagnetite biochar composite with siltstone

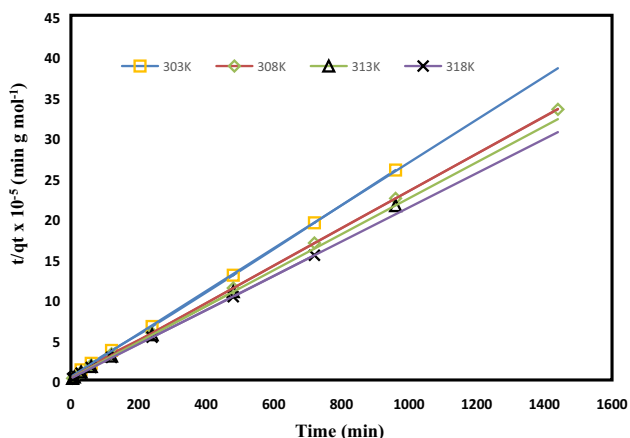


Fig. 10 Pseudo second order plot for chromium adsorption on nano-magnetite biochar composite with siltstone at pH 7

$$t/qt = 1/k_2q^2e + t/q \tag{2}$$

Here q_e indicates equilibrium concentration of metal ions whereas q_t is the concentration of metal ions adsorbed at time t . Figure 10 indicates a plot of t/qt versus t for Cr (VI) ions adsorption on magnetite biochar composite and a straight line is obtained from the plot. Intercept and slope of the straight line were used to calculate the values of k_2 and q_e . Higher value of R^2 ($=0.99$) shows that Cr (VI) ions adsorption on biochar composite is explained well by pseudo second order rate equation. The applicability of the pseudo second order model for Cr (VI) ions adsorption suggest the chemical nature of the process [42, 43].

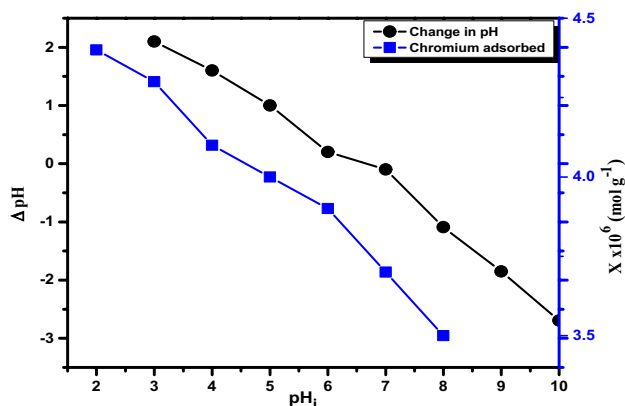


Fig. 11 Plots of ΔpH and chromium adsorbed vs pH_i by composite of nanomagnetite with siltstone at 303 K and initial concentration of 70 mg L^{-1}

3.10 Effect of pH on Adsorption of Chromium

The effect of pH on the adsorption of chromium by composite of magnetite biochar with siltstone was studied in the pH range of 2 to 8 at an initial concentration of 70 mg L^{-1} and is shown in Fig. 11. The graph shows strong pH dependency of chromium ions on the surface of the adsorbent. Adsorption was noted to decrease with rise of pH which can be explained by the speciation of chromium(VI) under different conditions of pHs. Cr(VI) exist dominantly as HCrO_4^{1-} in the lower pH range which is converted into CrO_4^{2-} and $\text{Cr}_2\text{O}_7^{2-}$ with the increase of pH [42, 44]. Maximum adsorption was observed at pH 2 which may be due to the electrostatic attraction between pre-PZC protonated surface of biochar composite and negatively charged chromium species (HCrO_4^{1-}). Increase of pH resulted in repulsion between negatively charged chromium ions (CrO_4^{2-} and $\text{Cr}_2\text{O}_7^{2-}$) and the post PZC (> 6.7) surface of the composite. Moreover, competition between increasing OH^{-1} and negative chromium species for the surface of the adsorbent also have an additional reductive effect on the adsorption of chromium at higher pH. Similar trend of chromium adsorption with varying pH was also reported by other researchers [45–47].

3.11 Effect of Temperature on Adsorption of Chromium

The effect of temperature on chromium adsorption by biochar composite in the initial concentration range of 10 to 100 mg L^{-1} and at pH 5 is shown in Fig. 12. Increased adsorption of chromium ions with the increase in the temperature can be observed from the Figure which is due to increase of adsorbent sites due to bond breakage at edges. Moreover, increased diffusion of the chromium ions with the increase in temperature into the pores of the adsorbents also leads to enhanced adsorption of chromium on the surface of magnetite biochar composite with the siltstone. Similar

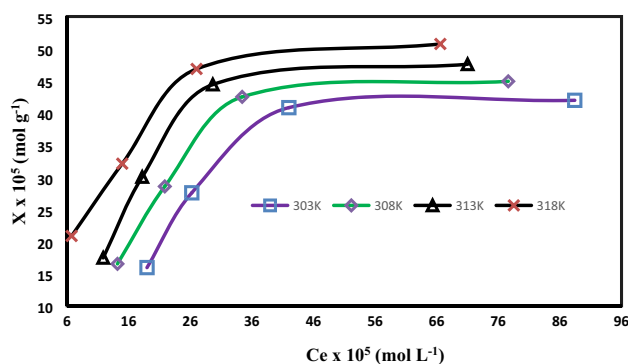


Fig. 12 Effect of temperature on the adsorption of chromium by composite of nanomagnetite with siltstone at pH 5

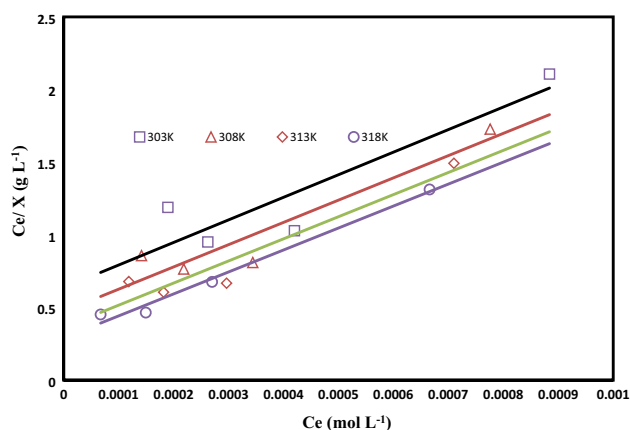


Fig. 13 Langmuir isotherm for chromium adsorption on nanomagnetite biochar composite with siltstone at pH 5

Table 1 Langmuir parameters for Cr (VI) ions adsorption on nanomagnetite biochar composite with siltstone at pH 5

Temp (K)	$X_m \times 10^5$ (mol g ⁻¹)	$K_b \times 10^{-5}$ (L mol ⁻¹)	R^2
303	64.52	2439.32	0.822
308	65.35	3240.27	0.8892
313	65.78	4185.04	0.9188
318	66.22	5195.53	0.9858

increase of chromium adsorption at higher temperature is reported elsewhere [48, 49].

3.12 Langmuir Equation

Langmuir adsorption assumes the adsorption to be monolayer. The adsorption data was tested by the well-known Langmuir equation in its linearized form as follow

$$\frac{C_e}{X} = \frac{1}{K_b X_m} + \frac{C_e}{X_m} \quad (3)$$

Table 2 Comparison of the adsorption capacities of different adsorbents for Cr(VI)

Adsorbent	X_m (mg g ⁻¹)	References
Sun flower stem waste	4.9	[61]
Polyaniline-coated electro spun membrane	15.08	[62]
Zeolitic imidazolate framework-67 microcrystals	13.34	[63]
NiFe layered double hydroxide	26.78	[64]
Corn straw biochars	26.18	[65]
Mn-doped zirconium metal-organic framework as	32.77	[66]
Nanomagnetite biochar composite with siltstone	35.57	Present study

Table 3 Comparison of thermodynamic parameters for chromium adsorption on MBS

Temp (K)	ΔG° (kJ mol ⁻¹)	ΔH° (kJ mol ⁻¹)	ΔS° (J mol ⁻¹ K ⁻¹)
303	-19.63		
308	-20.62	40.46	0.1983
313	-21.62		
318	-22.61		

where C_e shows the amount of adsorbate (mol L⁻¹) remaining in solution at equilibrium, X represents the amount of metal ions (mol g⁻¹) adsorbed and binding energy constant is represented by K_b (L mol⁻¹). The plot (C_e/X vs C_e) shows good linearity with higher values of R^2 (> 0.90) for all the temperatures under study (Fig. 13). Endothermic nature of the adsorption process was confirmed from the values of X_m (maximum adsorption capacity) which rises with rise of temperature as shown in Table 1. Same increase in binding energy with the increase in temperature was also observed. The X_m values are higher than the X_m values for different adsorbents (Table 2) reported in the literature [46, 50, 51].

3.13 Activation Energy

Linear form of Arrhenius equation can be used to calculate the energy of activation as shown below;

$$\ln k_2 = \ln A - E_a/RT \quad (4)$$

here A is the Arrhenius constant, k_2 is the rate constant for pseudo second order rate equation, R is the general gas constant and E_a is the activation energy for the adsorption of chromium ions. Activation energy from the linear plot ($R^2 = 0.991$) of Arrhenius equation (Fig. S2) was calculated to be 15.08 kJ mol⁻¹ which indicates the chemical nature of the process as it falls within the range (8.4–83.7 kJ mol⁻¹) of chemisorption process [52]. Moreover, the transport of chromate ions to the surface sites is controlled by the diffusion

process as suggested by the range ($< 42 \text{ kJ mol}^{-1}$) of activation energy [53].

3.14 Thermodynamic Parameters

The thermodynamic parameters for chromium adsorption on MBS were evaluated by using Eqs. 5 and 6 and are listed in Table 3.

$$\ln K_b = \frac{\Delta S^\circ}{R} - \frac{\Delta H^\circ}{RT} \quad (5)$$

$$\Delta G = \Delta H^\circ - T\Delta S^\circ \quad (6)$$

where R ($8.314 \times 10^{-3} \text{ J mol}^{-1} \text{ K}^{-1}$) is the general gas constant, T (K) is the temperature and K_b (L mol^{-1}) is the binding energy constant obtained from Langmuir equation. The value of ΔH° is found to be positive for chromium ions adsorption on MBS as calculated from Fig S3. The positive enthalpic values shows the endothermic behavior of chromium adsorption. The higher value of ΔH° ($40.46 \text{ kJ mol}^{-1}$) indicates that chemisorption may be responsible for the adsorption of chromium ions on the surface of MBS as enthalpy change for the chemisorption is $> 29 \text{ kJ mol}^{-1}$ [48, 54, 55].

Similarly, the non-negative values of entropy (ΔS°) for chromium ion adsorption suggest increased randomness at solid liquid interface. The value of entropy change is greater than zero which suggest increased disorder and degree of freedom at solid liquid interface indicating that adsorption process produces structural changes [44, 56]. The Gibbs free energy (ΔG°) values are negative and their negative magnitude increases with the rise of temperature which shows that adsorption process for chromium is feasible and spontaneous and also indicates that higher temperature favours the adsorption process [56].

3.15 Spectroscopic Evidence for Adsorption Mechanism

Post adsorption FTIR of the MBS (Fig. 2c) showed adsorption of chromium due to the functional groups on the surface of MBS. The peaks at 1635 and 1385 cm^{-1} for COO^- were suppressed which shows the involvement of carboxylate group in chromium adsorption and surface complexation and this result is in agreement with previous studies [57, 58]. In order to investigate the mechanism for the adsorption of hexavalent chromium pre and post adsorption XPS was performed (Fig. 14a, b). XPS analysis showed the presence of both Cr(III) and Cr(VI) on the surface of MBS. The Cr $2p_{1/2}$ band was detected at binding energy of $587\text{--}588 \text{ eV}$ whereas Cr $2p_{3/2}$ band appeared at

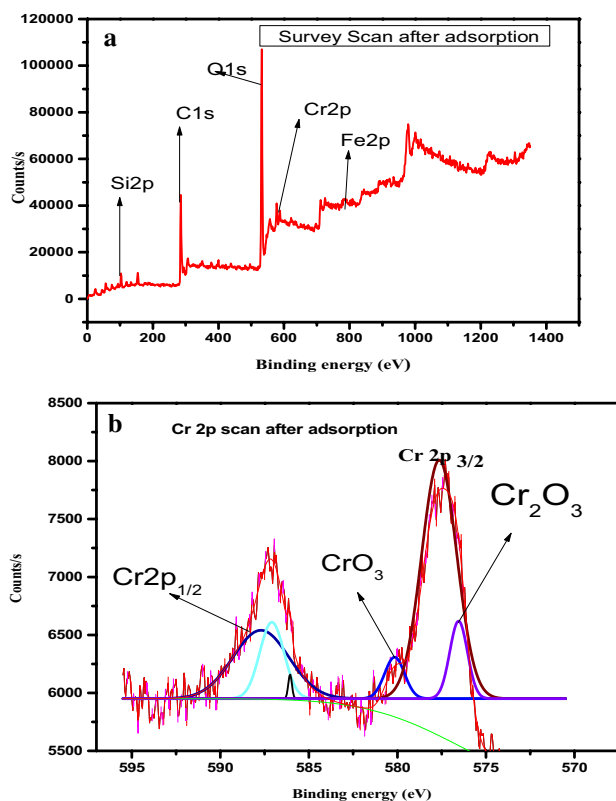


Fig. 14 XPS Survey scan of chromium loaded nanomagnetite biochar composite with siltstone (a) and XPS scan of Cr 2p in chromium loaded nanomagnetite biochar composite with siltstone (b)

$577\text{--}580 \text{ eV}$ [59] which was used to determine the valance state of chromium as shown in Fig. 14b. Some trivalent chromium Cr(III) was present at 577.2 eV and 576.2 eV [57]. This suggest reduction of hexavalent chromium to the trivalent chromium Cr(III) which then subsequently may make complexes with the functional groups of MBS [55, 59]. Similarly the hexavalent chromium peaks appeared at higher binding energy of 580.1 eV [60]. This suggests that positively charged surface of MBS (due to carboxylic, hydroxyl or alcohol) under strong acidic conditions have attracted the negatively charged Cr(VI) species [48]. Thus XPS results showed that MBS has effectively removed Cr(VI) with electrostatic attraction coupled with the reduction of Cr(VI) to Cr(III).

4 Conclusion

Composite of *Eleocharis dulcis* biochar (EDB) with nanomagnetite and siltstone was used to remove chromium from water. The XRD confirmed magnetite and quartz to be the main phases in the sample. The adsorbent particle size was found to be in the nano-range (18.5 nm) which was supported by the particles size calculated using TEM data. TGA

studies showed nanomagnetite biochar composite with siltstone to be stable at higher temperatures as compared to the nanomagnetite biochar justifying the addition of siltstone to the composite. Furthermore, the FTIR confirmed magnetite and silicon to be in the sample by showing extra peaks in the spectra. The oxidation states of iron and oxygen in the XPS confirmed iron to be in the magnetite form whereas the peak for Si shows its oxides to be mainly in the SiO₂ form. Lower pH range was found to be favorable for chromium adsorption. Endothermic nature of the adsorption system under investigation was confirmed by the increases in adsorption with the increase in temperature. Pseudo second order equation for chromium was obeyed by kinetic data whereas the adsorption data followed Langmuir equation. The thermodynamic parameters reveals the endothermicity and spontaneity of the adsorption process. The post XPS analysis showed that MBS has effectively removed Cr(VI) with electrostatic attraction coupled with the reduction of Cr(VI) to Cr(III).

Acknowledgements Salah Ud Din is thankful to the Higher Education Commission of Pakistan for research funding under National research program for universities (NRPU) under Project No. 8376.

References

1. J. Yang, B. Hou, J. Wang et al., Nanomaterials for the removal of heavy metals from wastewater. (2019). <https://doi.org/10.3390/nano9030424>
2. H. Park, L.L. Tavlarides, Adsorption of chromium(VI) from aqueous solutions using an imidazole functionalized adsorbent. *Ind. Eng. Chem. Res.* **47**, 3401–3409 (2008)
3. M.A.K. Saravanakumar, E.J.V. Muthuraj, Synthesis and characterization of 1D-MoO₃ nanorods using *Abutilon indicum* extract for the photoreduction of hexavalent chromium. *J Inorg Organomet Polym Mater* (2018). <https://doi.org/10.1007/s10904-018-0970-0>
4. J. Ifthikar, J. Wang, Q. Wang et al., Highly efficient lead distribution by magnetic sewage sludge biochar: sorption mechanisms and bench applications. *Bioresour. Technol.* (2017). <https://doi.org/10.1016/j.biortech.2017.03.133>
5. N.M. Mubarak, J.N. Sahu, E.C. Abdullah, N.S. Jayakuamr, Plum oil empty fruit bunch based magnetic biochar composite comparison for synthesis by microwave-assisted and conventional heating. *J. Anal. Appl Pyrolysis* (2016). <https://doi.org/10.1016/j.jaap.2016.06.026>
6. B. Zhang, Y. Wu, Y. Fan, Synthesis of novel magnetic-NiFe₂O₄ nanocomposite grafted chitosan and the adsorption mechanism of Cr(VI). *J. Inorg. Organomet. Polym. Mater.* (2018). <https://doi.org/10.1007/s10904-018-0987-4>
7. Y. Dong, *RSC Adv.* (2019). <https://doi.org/10.1039/c9ra05251h>
8. J. Han, G. Zhang, L. Zhou et al., Interfaces: adsorption, reactions, films, forces, measurement techniques, charge transfer, electrochemistry, electrocatalysis, energy production and storage waste carton-derived nanocomposites for efficient removal of hexavalent chromium. (2018). <https://doi.org/10.1021/acs.langmuir.8b00225>
9. C. Imawan, Y. Pr, Synthesis of C-4-hydroxy-3-methoxyphenyl calix[4] resorcinarene and its application as adsorbent for lead(II), copper(II) and chromium(III). *Bull. Chem. Soc. Jpn.* **92**, 825–831 (2019). <https://doi.org/10.1246/bcsj.20180323>
10. M. Imran, A.U. Islam, M.A. Tariq et al., Synthesis of magnetite-based nanocomposites for effective removal of brilliant green dye from wastewater. *Environ. Sci. Pollut. Res.* **26**, 24489–24502 (2019)
11. M.I. Inyang, B. Gao, Y. Yao et al., A review of biochar as a low-cost adsorbent for aqueous heavy metal removal. *Crit. Rev. Environ. Sci. Technol.* **46**, 406 (2015). <https://doi.org/10.1080/10643389.2015.1096880>
12. J. Ji, H. Xiong, Z. Zhu et al., Fabrication of polypyrrole/chitosan nanocomposite aerogel monolith for removal of Cr(VI). *J. Polym. Environ.* **26**, 1979–1985 (2018). <https://doi.org/10.1007/s10924-017-1095-1>
13. M.E. Mahmoud, G.M. Nabil, S.M.E. Mahmoud, Journal of environmental chemical engineering high performance nano-zirconium silicate adsorbent for efficient removal of copper(II), cadmium(II) and lead(II). *Biochem. Pharmacol.* (2014). <https://doi.org/10.1016/j.jece.2014.11.027>
14. A.H. Sulaymon, B.A. Abid, J.A. Al-Najar, Removal of lead copper chromium and cobalt ions onto granular activated carbon in batch and fixed-bed adsorbents. *Chem. Eng. J.* **155**, 647–653 (2009). <https://doi.org/10.1016/j.cej.2009.08.021>
15. S.S. Thavamani, R. Rajkumar, Removal of Cr(VI), Cu(II), Pb(II) and Ni(II) from aqueous solutions by adsorption on alumina. *Res. J. Chem. Sci.* **3**, 44–48 (2013)
16. X. Tuo, B. Li, X. Yu et al., Facile synthesis of magnetic polypyrrole composite nanofibers and their application in Cr(VI) removal. *Poly. Compos.* **39**, 1507–1513 (2016)
17. P. Wang, I.M.C. Lo, Synthesis of mesoporous magnetic g-Fe₂O₃ and its application to Cr(VI) removal from contaminated water. *Water Res.* **43**, 3727–3734 (2009). <https://doi.org/10.1016/j.watres.2009.05.041>
18. Y. Wu, H. Pang, Y. Liu et al., Environmental remediation of heavy metal ions by novel-nanomaterials: a review. *Environ. Pollut.* **246**, 608–620 (2019). <https://doi.org/10.1016/j.envpol.2018.12.076>
19. L. Yan, L. Kong, Z. Qu, et al., Magnetic biochar decorated with ZnS nanocrystals for Pb(II) removal (2014).
20. P.N. Dave, L.V. Chopda, Application of iron oxide nanomaterials for the removal of heavy metals. *J. Nanotechnol.* (2014). <https://doi.org/10.1155/2014/398569>
21. Z. Wan, D.-W. Cho, D.C.W. Tsang et al., Concurrent adsorption and micro-electrolysis of Cr(VI) by nanoscale zerovalent iron/biochar/Ca-alginate composite. *Environ. Pollut.* (2019). <https://doi.org/10.1016/j.envpol.2019.01.047>
22. T.S.A. Islam, Y. Zaker, M.A. Hossain, M.S. Islam, Physico-chemical characterization of silt prepared from Bijoypur soil. *J. Asiatic Soc. Bangl.* **39**, 53–60 (2013)
23. M.I. Majeed, J. Guo, W. Yan, B. Tan, Preparation of magnetic iron oxide nanoparticles (MIONs) with improved saturation magnetization using multifunctional polymer ligand. *Polymers (Basel)* **8**, 1–16 (2016). <https://doi.org/10.3390/polym8110392>
24. E.N. Bakatula, D. Richard, C.M. Neculita, G.J. Zagury, Determination of point of zero charge of natural organic materials. *Environ. Sci. Pollut. Res.* **25**, 7823–7833 (2018). <https://doi.org/10.1007/s11356-017-1115-7>
25. M. Rama Chandraiah, Facile synthesis of zero valent iron magnetic biochar composites for Pb(II) removal from the aqueous medium. *Alexandria Eng. J.* **55**, 619–625 (2016). <https://doi.org/10.1016/j.aej.2015.12.015>
26. C. Tan, Z. Zeyu, X. Sai et al., Adsorption behavior comparison of trivalent and hexavalent chromium on biochar derived from municipal sludge. *Bioresour. Technol.* (2015). <https://doi.org/10.1016/j.biortech.2015.04.115>
27. X. Tan, Y. Liu, G. Zeng et al., Application of biochar for the removal of pollutants from aqueous solutions. *Chemosphere* **125**, 70–85 (2015). <https://doi.org/10.1016/j.chemosphere.2014.12.058>

28. S. Ud, D. Ajmal, A. Zain et al., Investigation on cadmium ions removal from water by a nanomagnetite based biochar derived from *Eleocharis dulcis*. *J. Inorg. Organomet. Polym. Mater.* (2020). <https://doi.org/10.1007/s10904-020-01758-5>
29. M. Luo, H. Lin, B. Li et al., A novel modification of lignin on corncob-based biochar to enhance removal of cadmium from water. *Bioresour. Technol.* **259**, 312–318 (2018). <https://doi.org/10.1016/j.biortech.2018.03.075>
30. K.H. Shah, S. Ali, M. Waseem et al., Native and magnetic oxide nanoparticles (Fe_3O_4) impregnated bentonite clays as economic adsorbents for Cr(III) removal. *J. Solution Chem.* **48**, 1640–1656 (2019). <https://doi.org/10.1007/s10953-019-00912-z>
31. M. Waseem, S. Mustafa, A. Naeem et al., Physicochemical properties of mixed oxides of iron and silicon. *J. Non Cryst. Solids* **356**, 2704–2708 (2010). <https://doi.org/10.1016/j.jnoncrysol.2010.09.055>
32. N. Thi, V. Hoan, N. Thi et al., Fe_3O_4 /reduced graphene oxide nanocomposite: synthesis and its application for toxic metal ion removal. *J. Chem.* **2016**, 1–10 (2016). <https://doi.org/10.1155/2016/2418172>
33. L. Yang, J. Tian, J. Meng, et al., Modification and characterization of Fe_3O_4 nanoparticles for use in adsorption of alkaloids. (2018). <https://doi.org/10.3390/molecules23030562>.
34. X. Zhang, L. Zhang, A. Li, Eucalyptus sawdust derived biochar generated by combining the hydrothermal carbonization and low concentration KOH modification for hexavalent chromium removal. *J. Environ. Manag.* **206**, 989–998 (2018). <https://doi.org/10.1016/j.jenvman.2017.11.079>
35. D. Briggs, G. Beamson, XPS studies of the oxygen 1s and 2s levels in a wide range of functional polymers. *Anal. Chem.* **65**, 1517–1523 (1993). <https://doi.org/10.1021/ac00059a006>
36. Dong C, Chen C, Kao C, Chien C (2018) Remediation of PAH-contaminated estuary sediment. 1–13. <https://doi.org/https://doi.org/10.3390/catal8020073>
37. H. Lyu, J. Tang, Y. Huang et al., Removal of hexavalent chromium from aqueous solutions by a novel biochar supported nanoscale iron sulfide composite. *Chem. Eng. J.* **322**, 516–524 (2017). <https://doi.org/10.1016/j.cej.2017.04.058>
38. A. Miyakoshi, A. Ueno, M. Ichikawa, XPS and TPD characterization of manganese-substituted iron-potassium oxide catalysts which are selective for dehydrogenation of ethylbenzene into styrene. *Appl. Catal. A Gen.* **219**, 249–258 (2001). [https://doi.org/10.1016/S0926-860X\(01\)00697-4](https://doi.org/10.1016/S0926-860X(01)00697-4)
39. J.W. He, X. Xu, J.S. Corneille, D.W. Goodman, X-ray photoelectron spectroscopic characterization of ultra-thin silicon oxide films on a Mo(100) surface. *Surf Sci* **279**, 119–126 (1992). [https://doi.org/10.1016/0039-6028\(92\)90748-U](https://doi.org/10.1016/0039-6028(92)90748-U)
40. J.H. Kwon, L.D. Wilson, R. Samynaiken, Synthesis and characterization of magnetite and activated carbon binary composites. *Synth Met* **197**, 8–17 (2014). <https://doi.org/10.1016/j.synthmet.2014.08.010>
41. A. Shaaban, S. Se, N. Merry et al., Characterization of biochar derived from rubber wood sawdust through slow pyrolysis on surface porosities and functional groups. *Procedia Eng* **68**, 365–371 (2013). <https://doi.org/10.1016/j.proeng.2013.12.193>
42. H. Deveci, Y. Kar, Adsorption of hexavalent chromium from aqueous solutions by bio-chars obtained during biomass pyrolysis. *J. Ind. Eng. Chem.* **19**, 190–196 (2013). <https://doi.org/10.1016/j.jiec.2012.08.001>
43. J. Yang, M. Yu, W. Chen, Adsorption of hexavalent chromium from aqueous solution by activated carbon prepared from longan seed: kinetics, equilibrium and thermodynamics. *J. Ind. Eng. Chem.* **21**, 414–422 (2015). <https://doi.org/10.1016/j.jiec.2014.02.054>
44. I. Enniya, L. Rghioui, A. Jourani, Adsorption of hexavalent chromium in aqueous solution on activated carbon prepared from apple peels. *Sustain. Chem. Pharm.* **7**, 9–16 (2018). <https://doi.org/10.1016/j.scp.2017.11.003>
45. J.I.E. Chen, J. Shi, J. Tang, X. Lu, Removal of Cr(VI) and Cr(III) from aqueous solutions and industrial wastewaters by natural. *Environ. Sci. Technol.* **40**, 3064–3069 (2006). <https://doi.org/10.1021/es052057x>
46. T. Karthikeyan, S. Rajgopal, L.R. Miranda, Chromium(VI) adsorption from aqueous solution by Hevea Brasilinesis sawdust activated carbon. *J. Hazard. Mater.* **124**, 192–199 (2005). <https://doi.org/10.1016/j.jhazmat.2005.05.003>
47. Z. Khodaparast, S. Pashaei, S. Mohammadi et al., Fabrication of silver nanoparticles with antibacterial property and preparation of PANI/M/Al₂O₃/Ag nanocomposites adsorbent using biological synthesis with study on chromium removal from aqueous solutions. *J. Inorg. Organomet. Polym. Mater.* (2019). <https://doi.org/10.1007/s10904-019-01243-8>
48. D. Durano, A.W. Trochimczuk, U. Beker, Kinetics and thermodynamics of hexavalent chromium adsorption onto activated carbon derived from acrylonitrile-divinylbenzene copolymer. *Chem. Eng. J.* **187**, 193–202 (2012). <https://doi.org/10.1016/j.cej.2012.01.120>
49. E.K. Goharshadi, M.B. Moghaddam, Adsorption of hexavalent chromium ions from aqueous solution by graphene nanosheets: kinetic and thermodynamic studies. *Int. J. Environ. Sci. Technol.* **12**, 2153–2160 (2015). <https://doi.org/10.1007/s1376-2-014-0748-z>
50. D. Mohan, S. Rajput, V.K. Singh et al., Modeling and evaluation of chromium remediation from water using low cost bio-char, a green adsorbent. *J. Hazard. Mater.* **188**, 319–333 (2011). <https://doi.org/10.1016/j.jhazmat.2011.01.127>
51. G. Zelmanov, R. Semiat, Iron (Fe^{+3}) oxide/hydroxide nanoparticles-based agglomerates suspension as adsorbent for chromium (Cr^{+6}) removal from water and recovery. *Sep. Purif. Technol.* **80**, 330–337 (2011). <https://doi.org/10.1016/j.seppur.2011.05.016>
52. S.U. Din, T. Mahmood, A. Naeem et al., Detailed kinetics study of arsenate adsorption by a sequentially precipitated binary oxide of iron and silicon. *Environ. Technol.* (2017). <https://doi.org/10.1080/09593330.2017.1385649>
53. S.S. Baral, S.N. Das, P. Rath, Hexavalent chromium removal from aqueous solution by adsorption on treated sawdust. *Kinetics* **31**, 216–222 (2006). <https://doi.org/10.1016/j.bej.2006.08.003>
54. S. Ud, T. Mahmood, A. Naeem et al., A novel insight into the adsorption interactions of arsenate with a Fe-Si binary oxide. *Colloid J.* **81**, 469–477 (2019). <https://doi.org/10.1134/S1061933X19040045>
55. J. Zhou, Y. Wang, J. Wang et al., Effective removal of hexavalent chromium from aqueous solutions by adsorption on mesoporous carbon microspheres. *J. Colloid Interface Sci.* **462**, 200–207 (2016). <https://doi.org/10.1016/j.jcis.2015.10.001>
56. F. Zhu, S. Ma, T. Liu, X. Deng, Green synthesis of nano zero-valent iron/Cu by green tea to remove hexavalent chromium from groundwater. *J. Clean Prod.* **174**, 184–190 (2018). <https://doi.org/10.1016/j.jclepro.2017.10.302>
57. B. Choudhary, D. Paul, A. Singh, T. Gupta, Removal of hexavalent chromium upon interaction with biochar under acidic conditions: mechanistic insights and application. *Environ. Sci. Pollut. Res.* **24**, 16786–16797 (2017). <https://doi.org/10.1007/s11356-017-9322-9>
58. S. Xu, W. Yu, S. Liu et al., Adsorption of hexavalent chromium using banana pseudostem biochar and its mechanism. *Sustain* (2018). <https://doi.org/10.3390/su10114250>
59. L. Zhou, Y. Liu, S. Liu et al., Investigation of the adsorption-reduction mechanisms of hexavalent chromium by ramie biochars of different pyrolytic temperatures. *Bioresour. Technol.* **218**, 351–359 (2016). <https://doi.org/10.1016/j.biortech.2016.06.102>
60. X. Dong, L.Q. Ma, Y. Li, Characteristics and mechanisms of hexavalent chromium removal by biochar from sugar beet tailing. *J.*

- Hazard. Mater. **190**, 909–915 (2011). <https://doi.org/10.1016/j.jhazmat.2011.04.008>
61. M. Jain, V.K. Garg, K. Kadirvelu, Chromium(VI) removal from aqueous system using *Helianthus annuus* (sunflower) stem waste. J. Hazard. Mater. **162**, 365–372 (2009). <https://doi.org/10.1016/j.jhazmat.2008.05.048>
62. G. Dognani, P. Hadi, H. Ma et al., Effective chromium removal from water by polyaniline-coated electrospun adsorbent membrane. Chem. Eng. J. **372**, 341–351 (2019). <https://doi.org/10.1016/j.cej.2019.04.154>
63. X. Li, X. Gao, L. Ai, J. Jiang, Mechanistic insight into the interaction and adsorption of Cr(VI) with zeolitic imidazolate framework-67 microcrystals from aqueous solution. Chem Eng J **274**, 238–246 (2015). <https://doi.org/10.1016/j.cej.2015.03.127>
64. Y. Lu, B. Jiang, L. Fang et al., High performance NiFe layered double hydroxide for methyl orange dye and Cr(VI) adsorption. Chemosphere **152**, 415–422 (2016). <https://doi.org/10.1016/j.chemosphere.2016.03.015>
65. N. Zhao, Z. Yin, F. Liu et al., Environmentally persistent free radicals mediated removal of Cr(VI) from highly saline water by corn straw biochars. Bioresour. Technol. **260**, 294–301 (2018). <https://doi.org/10.1016/j.biortech.2018.03.116>
66. Z. Yang, J. Cao, Y. Chen et al., Mn-doped zirconium metal-organic framework as an effective adsorbent for removal of tetracycline and Cr(VI) from aqueous solution. Microporous Mesoporous Mater. **277**, 277–285 (2019). <https://doi.org/10.1016/j.micromeso.2018.11.014>

Publisher's Note Springer Nature remains neutral with regard to jurisdictional claims in published maps and institutional affiliations.